Journal of
Ceramic Science
and Technology

J. Ceram. Sci. Tech., **05** [03] 223-236 (2014)
DOI: 10.4416/JCST2014-00011
available online at: http://www.ceramic-science.com

Thermoplastic Forming as an Alternative Shaping Process for Near-Net-Shape Production of C-SiSiC Ceramics via Liquid Silicon Infiltration (LSI) Process

S. Weber*[1], F. Sommer[2], F. Kern[2], R. Gadow[2], H. Voggenreiter[1], D. Koch[1]

[1]Institute of Structures and Design, Dep. Ceramic Composites and Structures, German Aerospace Center (DLR), Pfaffenwaldring 38 – 40, D-70569 Stuttgart, Germany
[2]Institute for Manufacturing Technologies of Ceramic Components and Composites, University of Stuttgart, Allmandring 7b, D-70569 Stuttgart, Germany
received March 12, 2014; received in revised form May 7, 2014; accepted May 25, 2014

Abstract

The present study demonstrated the feasibility of producing carbon-based green bodies by means of extrusion, pyrolysis and subsequent conversion to C-SiSiC ceramics according to the LSI process. A thermoplastic binder system was used for the development of feedstocks that differ from conventional duroplastic binder systems as these would have created difficulties during processing owing to their curing behavior. Activated carbon, carbon fibers and semi-coke were used as fillers and a source of a sufficiently stable carbon backbone in the carbonized intermediate. Special attention was paid to the characterization and quantification of material behavior at the water debinding step as well as at thermal treatment during pyrolysis. Porosity and microstructural characteristics of carbon bodies and subsequent C-SiSiC microstructure after Si-infiltration were investigated by means of scanning electron microscopy and porosity measurements. The feasibility of producing carbon-based extrusion feedstocks with high homogeneity and flowability which can be converted into SiC by means of LSI shows that the concept may be applied to production of near-net-shape C-SiSiC components by means of thermoplastic injection molding.

Keywords: Extrusion, injection molding, SiC, porosity, feedstock system

I. Introduction

Silicon carbide (SiC) exhibits favorable thermal and chemical characteristics, such as a high melting point, good thermal conductivity, superior oxidation and corrosion resistance. Furthermore, SiC provides exceptional wear resistance, high strength and hardness. These characteristics make silicon-carbide-based ceramics attractive candidates for structural applications in heating, tribological and ballistic components [1–6, 17, 18].

Commercially available SiC products are mainly produced with different sintering methods such as pressureless (SSiC) and pressure-assisted (HPSiC) sintering, and liquid phase sintering (LPSiC) technique. For all these methods, SiC powders with highly covalent Si-C bonds and sintering aids such as carbon, aluminium, boron or yttrium are required as raw materials. Sintering temperatures for SiC derived from powder technology range from 1875 °C for LP-SiC up to 2500 °C for recrystallized SiC (RSiC) [1, 2, 19–21]. Net-shape production can be accomplished by pressing technology, more complex-shaped parts can be obtained by green machining, in most cases the parts require a costly final machining step of functional surfaces to match dimensional tolerances and obtain good mechanical properties.

* Corresponding author: steffen.weber@dlr.de

The manufacture of reaction-formed SiC-based ceramics via liquid silicon infiltration (LSI) of carbon preforms is a well-known process technique, which has been extensively studied in the past. In these studies, the use of cellulosic- and resin/glycol-precursors for carbon preform processing was demonstrated and assessed with regard to a high silicon carbide yield. A combination of different carbon precursors was suitable to achieve carbon preforms with densities and porosities for an effective infiltration and reaction mechanism [3–18]. First experiments, focusing on the extrusion of cellulosic precursors, showed the possibility of near-net-shape manufacture of green bodies for the subsequent LSI process [22]. However, the successful manufacture of reaction-formed SiC-based ceramics is often assessed one-dimensionally, ignoring the interaction between the reaction/infiltration mechanism and the role of processability during the multistage LSI process.

The LSI process has several advantages such as the possibility of near-net-shape production of components at low process temperatures ($T > 1400$ °C) in contrast to sintering methods. Furthermore, the silicon infiltration of carbon preforms may be performed without supplied pressures using capillary forces, which can also reduce the expenditure of process energy. These facts enable efficient and low-cost production of SiC-based ceramics.

This work is focused on the development of carbon preforms via extrusion and infiltration of these preforms with liquid silicon to form C-SiSiC ceramics. Thermoplastic forming processes such as extrusion or injection molding are suitable processes for an upcoming series production of complex-shaped components. For oxide ceramics it was shown that similar feedstock compositions can be used for both extrusion and injection molding [23, 24].

Challenges were the feedstock development for the structure formation and the further processing of the thermoplastic preforms in the established LSI route. In this approach, feedstock systems based on a thermoplastic binder and carbon fillers (activated carbon, carbon fibers and semi-coke) were generated and shaped by means of extrusion. A subsequent debinding process, consisting of a pre-debinding step in a water solution and thermal debinding step (pyrolysis) up to temperatures of 1650 °C, enabled the production of highly porous carbon preforms. The relation between the carbon matrix and porosity (e.g. apparent porosity, pore size and pore size distribution) influenced mainly the formation of the C-SiSiC ceramic microstructure.

Reactive carbon fillers with high specific surface area and an appropriate amount of silicon are necessary for the reaction mechanism between reactive elements and for silicon carbide yield after the liquid silicon infiltration. The porosity formation during the debinding steps, carbon conversion and the morphology of the resulting carbon matrix determine the infiltration degree of carbon preforms and were thus extensively investigated in this work. To manufacture silicon-carbide-based ceramics, the carbon preforms were infiltrated by liquid silicon above temperatures of the silicon melting point. The C-SiSiC microstructures obtained were correlated to the characteristics of the corresponding initial carbon preforms. Finally, tribological investigations were conducted in order to compare the C-SiSiC ceramics and the different phase compositions.

Summarizing, this study is focused on the development of highly porous and reactive carbon preforms via a forming process with high densification of the material. In this context, thermoplastic feedstock systems (based on high reactive activated carbon) are developed for an extrusion/injection molding process to obtain stable green and carbon preforms with the appropriate carbon content, porosity and pore size distribution. Furthermore, recipes with variation in binder and filler content were produced to establish correlations between the structure and composition of the green bodies and the final reaction-bonded C-SiSiC material systems.

II. Experimental/Processing and Characterization

(1) Manufacturing process and raw materials

Three C-SiSiC material configurations, based on one type of thermoplastic binder system and carbon additives as fillers, were produced according to a four-stage process. This process is divided into the basic steps compounding, shaping, debinding/carbon conversion and siliconization (Fig. 1). In this case, structure formation was realized by means of an extrusion process and subsequent two-stage debinding-process (referred to as Route 1 and 2 in Fig. 1), considering the optional injection molding process. A distinction is made between thermal debinding with separate water debinding (Route 1) step, which enables delicate removal and conversion of the binder system, and direct thermal debinding (Route 2).

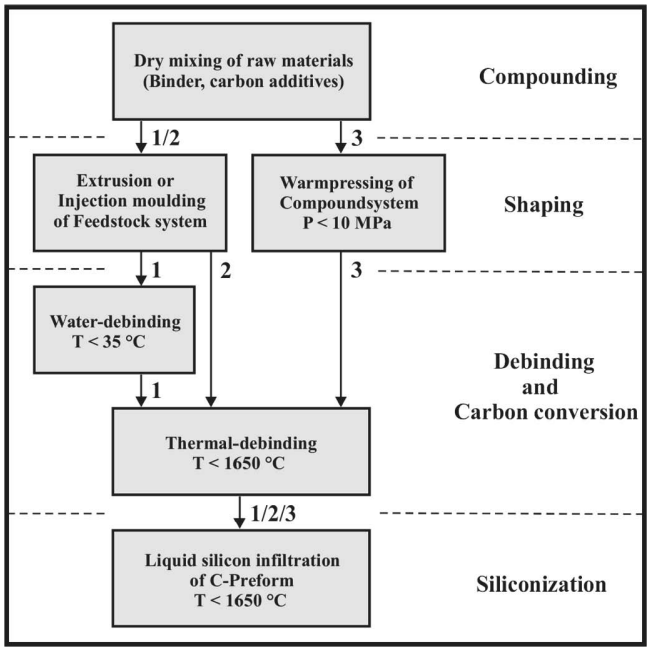

Fig. 1: Schematically illustration of the four stage process to produce C-SiSiC ceramics via liquid silicon infiltration and previous carbon preform manufacture. Three possible processing routes are illustrated and labeled with 1, 2 and 3. This work includes route 1 and 2.

As primary binding agent, the commercial thermoplastic binder (Licomont EK 583 G, eMBe Products & Service GmbH, Germany) was used, with a melting temperature of ~ 100 °C. A coal-tar-pitch-based sinterable semi-coke (Carbosint, Rütgers Chemicals AG, Germany) acted as secondary binder agent and additional carbon backbone. Its average particle size was below 10 μm. Activated carbon powder (RD-90, Chemviron Carbon, Belgium) with a specific surface of 1100 m²/g was added as a further filler material. The activated carbon particles have an average diameter of 10 μm and are spherical in shape. Ground pitch-based carbon fibers (Ashland-Südchemie-Kernfest GmbH, Germany) with a mean diameter of 13 μm and an average fiber length of 360 μm served as the carbon source and additional stabilization element.

(2) Feedstock systems and extrusion process

In this study, three different feedstock systems labeled FS-1, FS-2 and FS-3 were manufactured and investigated to generate information about their processability. The realized feedstock compositions are listed in Table 1.

Initially, all powdery raw materials such as thermoplastic binder, semi-coke, activated carbon and carbon fibers of the projected compositions were pre-mixed to feedstocks FS-1, FS-2 and FS-3 (Table 1). The semi-coke was previously ground for the feedstock systems FS-2 and FS-3 in order to facilitate direct comparison of different particle sizes. To homogenize the feedstock systems, a rotary drum

mixer was used. The mixing time was set to approximately 10 minutes for each feedstock system.

Table 1: Volumetric raw material composition of feedstock system FS-1, FS-2 and FS-3.

Feedstock	Binder	Semi-coke	Activated carbon	Carbon fibers
	[vol.%]	[vol.%]	[vol.%]	[vol.%]
FS-1	35.0	35.2	9.0	19.8
FS-2	45.0	30.3	7.7	17.0
FS-3	48.3	23.5	11.2	17.0

The pre-mixed compositions were then passed three times through a twin-screw extruder (screw diameter 16 mm) without the mouthpiece (Thermofisher Scientific, Germany) at 140 °C to melt the binder and homogenize the pre-mix. Finally, the intensively pre-mixed granulate was fed into the same extruder and slowly extruded through a rod die (d = 12 mm) at 140 °C. The extrusion speed was limited by the specifications of the machine (torque below 60 Nm and pressure measured at the nozzle below 7.5 MPa). The rods obtained were supported by a V-track, cooled and cut into pieces for further processing.

(3) Debinding and siliconization step

Green bodies based on FS-1, FS-2 and FS-3 were pre-debinded over seven days in a water bath at 33 °C. In the following thermal-debinding step, *in-situ* carbon conversion (pyrolysis) was performed (Route 1, Fig. 1). The pyrolysis process was conducted at a heating rate of 15 K/h up to 900 °C and 100 K/h up to 1650 °C final temperature under flowing nitrogen atmosphere. During pyrolysis, the thermoplastic binder is completely evaporated while the semi-coke decomposes at high carbon yield, thus forming a carbon matrix including porosity together with the other fillers. The carbon conversion is combined with mass loss and shrinkage. To quantify the impact of the pre-debinding procedure, another batch of green bodies was directly thermally debinded (Route 2, Fig. 1) without the preceding water debinding. In the following elaboration, material configurations including water debinding are labeled "WD", materials derived from thermal debinding are labeled "TD" the materials which have passed both debinding steps are labeled "WD + TD".

After debinding and carbon conversion, the resulting carbon preforms were infiltrated with liquid silicon in a furnace at a heating rate of 130 K/h up to 1650 °C and a dwell of 30 min at final temperature to generate C-SiSiC ceramics. Afterwards, adhering silicon was removed by sandblasting of the specimen with corundum granulate.

(4) Characterization and testing

(a) *Raw materials and feedstock systems*

In order to investigate the thermal decomposition behavior of the raw materials and feedstocks (FS-1, FS-2 and FS-3), simultaneous thermal analysis (STA 409, Netzsch-Gerätebau GmbH, Selb, Germany) was conducted under a flowing nitrogen (100 ml/min) atmosphere. The heating rate was 10 K/min for a temperature range of 20...1500 °C.

(b) *Microstructure, density and porosity characterization*

The skeleton density of extruded green bodies, debinded carbon preforms and C-SiSiC ceramics was measured by means of a helium pycnometer (type: Accupyc 1330, Micromeritics Instrument Corporation, Norcross, Georgia, USA) acc. to ISO 1183. All measurements of green bodies and debinded carbon preforms were performed on milled material, to calculate open and closed pores, respectively. The green body skeleton density results were correlated with a theoretical approach calculated on the basis of raw material measurements and defined composition of feedstock systems:

$$\varrho_{green} = \varphi_1 \times \varrho_1 + \varphi_2 \times \varrho_2 + \ldots \varphi_n \times \varrho_n \quad (1)$$

where ϱ_{green} is the skeleton density of the green body, φ and ϱ the percentage volume share and skeleton density of the raw material components.

For the LSI process and the associated silicon infiltration, the carbon yield [vol%] of a green body is necessary to obtain a certain porosity. The ceramic yield of feedstock systems for a pyrolysis temperature of 1500 °C under nitrogen atmospheres was calculated with the results of TGA and density of green, water-debinded (WD) and water-debinded + thermal-debinded (WD + TD) material as follows:

$$K_C = \frac{K_{C,TGA}}{100\,wt.\%} \times \frac{\frac{\rho_{green}}{WD}}{\rho_{WD+TD}} \times 100\,vol.\% \quad (2)$$

where K_C is the carbon yield [vol%], $K_{C,TGA}$ is the mass yield [wt%] from TGA, ϱ_{green}, ϱ_{WD} and ϱ_{WD+TD} is the skeleton density [g/cm³] of the green body, water-debinded and pyrolysed material, respectively. It should be noted that the calculated carbon yield is referenced to the total volume without existing porosity. It means that the percentage of carbon yield is in a direct relation to the new formed porosity. This correlation is explained in following equation, with V_{total} as total volume, V_P as already existing porosity, $V_{P,new}$ the volume of new formed porosity, which is asymptotic to the incurred carbon yield K_C:

$$V_{total} = (K_C + V_{P,new}) + V_P \quad (3)$$

Furthermore, the evolution of apparent density and open porosity of the material configurations (FS-1, FS-2 and FS-3) was monitored after each processing step with the Archimedes method acc. to DIN 51918.

Pore diameter distribution of each carbon preform after the water debinding and additional thermal debinding process (WD + TD) was measured by means of mercury intrusion porosimetry (type: Pascal 240, CE Instruments, Hindley Green, United Kingdom) acc. to DIN 66133. The pressure range was between 0.1...200 MPa. Hence, pore diameter between 10 nm and 100 μm could be determined. For calculation of pore diameters, a cylindrical pore shape model and a mercury contact angle of 140° was used.

C-SiSiC materials and prior intermediates formed after all debinding steps were examined by scanning electron microscope (SEM; type: Zeiss Ultra Plus, Carl Zeiss NTS

GmbH, Oberkochen, Germany). The SEM is equipped with an energy-dispersive spectroscopy (EDS) system (X-Max detector 20 mm², Oxford Instruments, Tubney Wood, United Kingdom).

(c) *Tribological properties*

For mechanical characterization, tribological tests were conducted with a pin-on-disk tribometer (IFKB, University Stuttgart, Germany) acc. to DIN 50324. Polished samples (20 mm^L x 6 mm^W x 5 mm^H) of each C-SiSiC material system were tested. Measurements were conducted in translational motion with 20 N normal load using a cemented carbide (WC/Co) ball of 5 mm diameter at a sliding speed of 0.012 m/s and a sliding distance of 10 mm. The number of strokes was 100 000 corresponding to a sliding distance of 2 000 m.

III. Results and Discussion

(1) Characterization of raw materials

In Fig. 2 TGA curves of used raw materials (thermoplastic binder, semi-coke, activated carbon and carbon fibers), which were dried for 24 hours at 40 °C under nitrogen atmosphere, are given for a temperature range of 20...1500 °C. The mass loss of the thermoplastic binder started at ~ 250 °C and was already finished at 550 °C with full material degradation. The mass loss of activated carbon as well as carbon fibers is below ~ 5 % up to a temperature of 1100 °C. At high temperature the activated carbon shows a significantly higher mass decrease gradient. The activated carbon, a bituminous coal-derived material containing many impurities, is produced at temperatures of < 1100 °C. Therefore a further increase in temperature leads to thermal decomposition and activation of the material. The main mass loss of semi-coke occurred between 250 °C and 900 °C (about~ 12 %) followed by a smaller but consistent mass decrease gradient.

The incipient mass loss is a result of elimination of organic groups, particularly for thermoplastic binder, evaporated as hydrocarbons, carbon oxides and hydrogen. Finally, the mass loss of the raw materials converged to their specific mass yield [wt%], which in turn is an important origin for total carbon yield and porosity evolution of carbon preform.

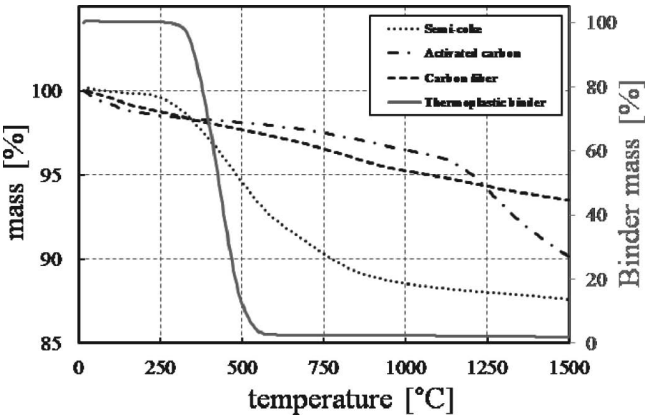

Fig. 2: TGA of raw material components (thermoplastic binder, carbon fillers and stabilization elements) under nitrogen atmosphere (temperature range: 20 – 1500 °C, heating rate: 10 K/min).

(2) Characterization of feedstock systems

The different feedstock systems show different processing characteristics during extrusion. Feedstock system FS-1, with only 36 vol% thermoplastic binder content, resulted in poor processability owing to its high viscosity. Extrusion of this feedstock system was possible, however, cracks occurred on the extruded solid rod surfaces. Owing to the high occurring torque and shear forces during processing, the material surfaces break up. Increasing the binder content up to 45 vol% and 48.3 vol% for feedstock system FS-2 and FS-3 enabled superior processability of both systems with lower torque, shear forces and associated lower viscosity. Even the increase of activated carbon content and simultaneous decrease of secondary binder agent in form of the semi-coke, did not significantly influence the processability of feedstock system FS-3.

Fig. 3 shows TGA measurements of the feedstock systems in the green state (FS-1, FS-2 and FS-3) and the water-debinded state (FS-1-WD, FS-2-WD and FS-3-WD). The samples were measured in a nitrogen atmosphere at a temperature range of 20 – 1500 °C.

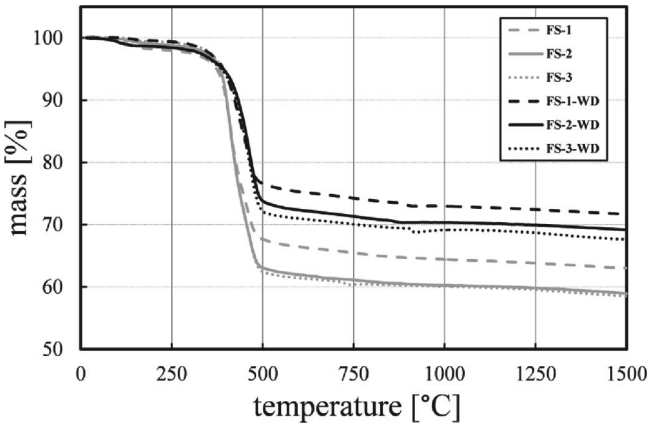

Fig. 3: TGA of feedstock systems in green body configuration (FS-1, FS-2, FS-3) and pre-debinded / water-debinded configuration under nitrogen atmosphere (temperature range: 20 – 1500 °C, heating rate: 10 K/min).

The analysis shows a similar decomposition material for all three feedstocks. The water-debinding materials show ~ 10 % lower weight loss than the green bodies. Taking into account the different densities of fillers and binder, the water-debinding step is capable of removing ~ 40 – 45 wt% of the binder fraction, a result in good accordance with previous results obtained on injection-molded oxide ceramics [21]. The mass loss corresponds very well to the initial compositions. Binder decomposition is the dominant effect making up ~ 90 % of the total mass loss, the second important mass loss is derived from pyrolysis of the semi-coke.

The main mass loss of each feedstock system finished at ~ 550 °C, which correlates with the mass loss of the thermoplastic binder and indicates its complete degradation. Beyond ~ 500 °C, the mass decrease gradient is nearly the same for each feedstock system. This comprises a mass loss of ~ 5 wt% over the temperature range of 500…1500 °C. Finally, the mass loss of the feedstock systems converged asymptotically to their specific mass yield [wt%].

Table 2: Skeleton densities after extrusion process (green), debinding steps and corresponding carbon yield of the feedstock systems.

Feedstock	[a]ϱ_{green}	[b]$\varrho_{green,calculated}$	[a]ϱ_{WD}	[a]ϱ_{TD}	[a]ϱ_{WD+TD}	$K_{C,\ TD}$	$K_{C,WD+TD}$
0	[g/cm³]	[g/cm³]	[g/cm³]	[g/cm³]	[g/cm³]	[vol.%]	[vol.%]
FS-1	1.42	1.44	1.45	1.64	1.67	54.55	62.24
FS-2	1.39	1.39	1.42	1.66	1.66	49.37	59.18
FS-3	1.40	1.40	1.43	1.62	1.63	50.56	59.33

[a] Density measured with the helium pycnometer according to ISO 1183
[b] Density calculated on the basis of feedstock composition (Equation 1)

(3) Formation of density, porosity and microstructure during extrusion and debinding

The results for the skeleton density of the green body, water-debinded, thermal-debinded and water + thermal-debinded material modifications, carbon yield after direct thermal-debinding as well as carbon yield after water + thermal-debinding (calculated with Equation 2) are summarized in Table 2. For reference, the green body skeleton density was determined with Equation 1 and compared to the values measured with the helium pycnometer.

Skeleton densities of green bodies, measured and calculated, were highly concordant. The marginal difference in the green body density of feedstock system FS-1 might be caused by the existence of closed pores, which could not be completely eliminated by milling. The influence of the pre-debinding/water-debinding step (degradation of water-soluble binder components) is reflected in the slightly increase of the appropriate skeleton density in contrast to the green body skeleton density. There are no significant differences in the skeleton density of materials generated by direct thermal-debinding and water + thermal-debinding, this result can be expected as the carbon yield of the binder is zero. The slight difference in skeleton density between each feedstock system is based on the differences in the raw material composition of the feedstock systems. The low skeleton density after both debinding routes of FS-3 can be explained by the lower starting content of secondary binder (semi-coke) and the increased amount of thermoplastic binder. This reduces the skeleton density owing to the higher amount of volatiles.

The calculated carbon yields of the water + thermal-debinded feedstock systems are nearly ~ 10 vol% higher than the carbon yields of direct thermal-debinded materials. This result of the pre-debinding/water-debinding procedure corresponds to the TGA measurements. This shows that the decomposition of the binder does not seem to interfere with the decomposition mechanism of the other constituents finally leading to identical density after debinding Route 1 and Route 2.

However, some effects concerning the bulk density and open porosity evolution can be attributed to the different debinding schemes. Fig. 4 shows the evolution of bulk density and open porosity of FS-1, FS-2 and FS-3 in the green body and debinded material modifications. The bulk density decreased for all materials, whereas the open porosity increased over the ongoing debinding Routes 1 and 2. Evidently for the FS-1 and FS-2 having the highest solid content and lowest porosity there is a difference in the porosity after debinding Routes 1 and 2. The WD + TD materials have higher bulk density and thus lower porosity than the purely TD materials. This may be caused by a slight bloating effect of the volatiles generated from the thermoplastic binder during decomposition, which increases the porosity.

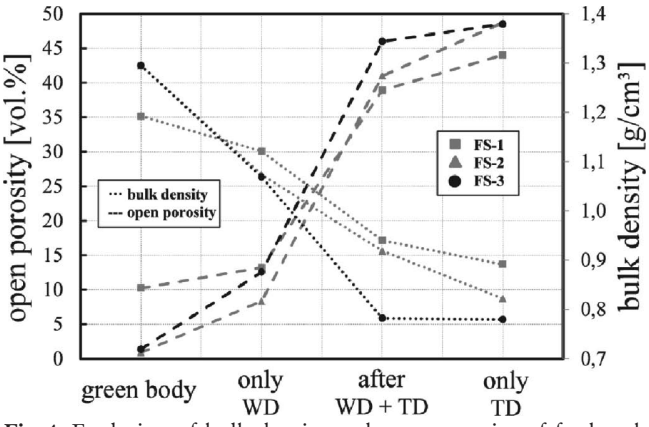

Fig. 4: Evolution of bulk density and open porosity of feedstock systems FS-1, FS-2 and FS-3 in green body, water-debinded (WD), water + thermal-debinded (WD+TD) and direct thermal-debinded (TD) material modification measured by Archimedes method according to DIN 51918.

The comparison of feedstock system FS-2 and FS-3 in green body modification indicates that after extrusion process, open porosity is similar and at a low level (0.88 vol% and 1.37 vol% for FS-2 and FS-3, respectively). This assumes very good densification and homogenization without any pores during the extrusion process. These results agree with the obtained microstructures from SEM analysis (Fig. 5a, c). The difference in open porosity of FS-1 after the extrusion process might be caused by slightly lower and probably insufficient thermoplastic binder content and resulting lower homogenization level. Generated surface cracks and a lower densification level of the microstructure of feedstock system FS-1 are reflected in open porosity values of ~ 10 vol% after the extrusion process.

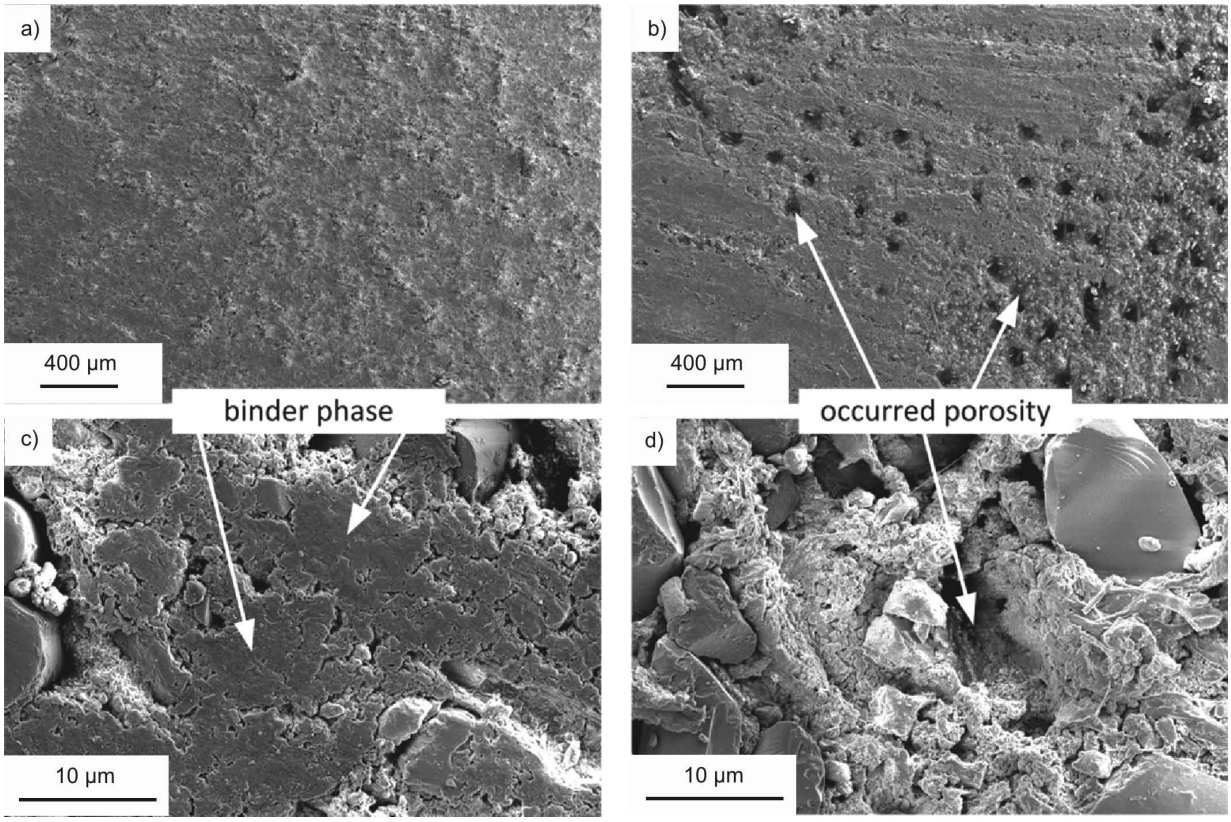

Fig. 5: SEM-micrographs (SE) of unpolished cross sections of FS-3 green body material after extrusion process (a, c) and after pre-debinding/water-debinding step (b, d).

The comparison of pre-debinded/water-debinded (WD) material modification indicates that the values of generated open porosity are in the range of ~ 8...14 vol%, which correlates very well with the water-soluble fraction of the thermoplastic binder content. In the case of the water-debinding process, sequential pore formation takes place. The occurring pores are distributed over the entire cross-section of specimens. In patches, stronger degradation of the thermoplastic binder could be observed in form of spherical pores, which is caused by increased partial accumulation of binder in these areas (Fig. 5b, d). Nevertheless, these compact areas are equally distributed over the cross-section of the extruded rods.

For water + thermal-debinded (WD + TD) as well as directly thermal-debinded (TD) feedstock materials the open porosity range was between 38…49 vol% and the corresponding bulk density between 0.78...0.94 g/cm³ (Fig. 4). In general, the open porosity is determined primarily by the volumetric content of thermoplastic binder within the feedstock systems. This is also demonstrated by the good agreement between the measured open porosity values and introduced volume amount of thermoplastic binder. However, it must be taken into account that a certain amount of nano-porosity and closed porosity, which could not be determined with the Archimedes method, will increase the measured total porosity. Nano-porosity is mainly caused by activated carbon and the main origin of its high specific inner surface. In the case of the directly thermal-debinded material modification (conforms to debinding Route 2), open porosities of FS-2 and FS-3 were not substantially different and were approximately ~ 48 vol%. In contrast to that, the feedstock system FS-1 shows a lower open porosity (~ 38 vol%). These two facts confirm that the thermoplastic binder content mainly influences the porosity and not the variation of carbon fillers.

Fig. 6 shows the microstructures of FS-1 (Fig. 6a, b), FS-2 (Fig. 6c, d) and FS-3 (Fig. 6e, f) after the water + thermal-debinding process step. In order to maintain the microstructure and for better illustration of porosity, the highly porous carbon preforms were stabilized with resin by means of infiltration of the open porosity. The local accumulations of porosity were well distributed after water + thermal-debinding as well as direct thermal-debinding and shows process-related vein-like structures (Fig. 6). These significant pore channels may reach diameters of ~ 50 µm and show a high degree of cross-linking with each other. The microstructures indicate some potential for improvement by means of better homogenization of the starting powders with the thermoplastic binder. Furthermore, the images clearly show the typical extrusion-process-derived anisotropy of the elongated fillers in the direction of flow. The anisotropy also has an impact on pore size distribution and orientation. The embedded carbon fiber can be easily recognized. The remaining carbon backbone consists of highly porous activated carbon and pitch-coke (Fig. 6b, d, f). Most of the carbon matrix areas exhibited finely distributed porosity and showed no or only very minor carbon cluster formation.

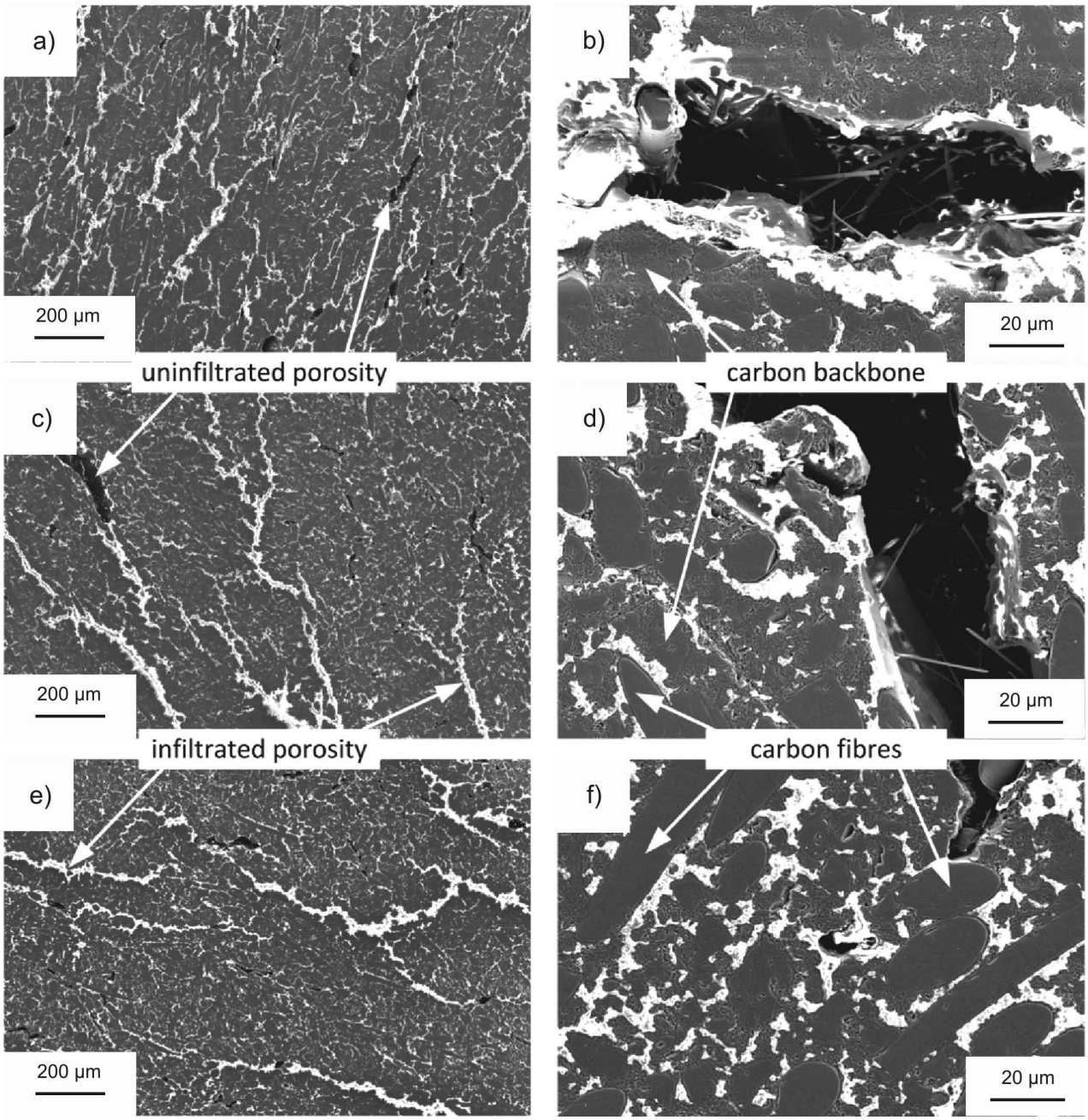

Fig. 6: SEM-micrographs (SE) of polished cross sections of water + thermal-debinded material, stabilized with resin (light colored) which is tantamount to the open porosity. Feedstock system FS-1 (a, b), FS-2, (c, d) and FS-3 (b, d) is faced.

Pore size distribution of all feedstock systems after the water + thermal-debinding process step was measured with mercury intrusion porosimetry (Fig. 7). Pore size distributions of the intermediates differ strongly especially in the case of FS-1. The feedstock system FS-1 shows a broad spectrum of pore size distribution. The maximum of the distribution is at ~ 10 µm, the distribution is not monomodal but has a shoulder towards finer pore sizes. 27 vol% of pores are smaller than 1 µm, the total porosity amounts to 520 mm³/g. The feedstocks FS-2 and FS-3 show similar shapes of pore size distribution, both distributions are monomodal. In the case of FS-2 the maximum is at a pore size of ~ 4 µm, only 16 vol% of pores are finer than 1 µm, the total porosity is 630 mm³/g. FS-3 has the highest porosity of 700 mm³/g, the maximum of the distribution is at ~ 3 µm, 25 vol% of pores are finer than 1 µm. Details of pore size distributions are shown in Table 3. The measured pore size distributions reflect the differences in the feedstock compositions, especially a variation in high surface-area-activated carbon content strongly influences pore size distribution in the < 100 nm range.

The results of mercury intrusion porosimetry (modal and average pore diameter as well as open porosity) are summarized in Table 3 and compared to open porosity measured with the Archimedes method. Open porosities measured by means of mercury intrusion porosimetry are larger than values measured with the Archimedes method, which correlates very well to the fact that pores smaller than 1 µm cannot be detected with the Archimedes method. Nevertheless, owing to the quite heterogeneous microstructure of the composites, a certain influence of measurement errors can be assumed.

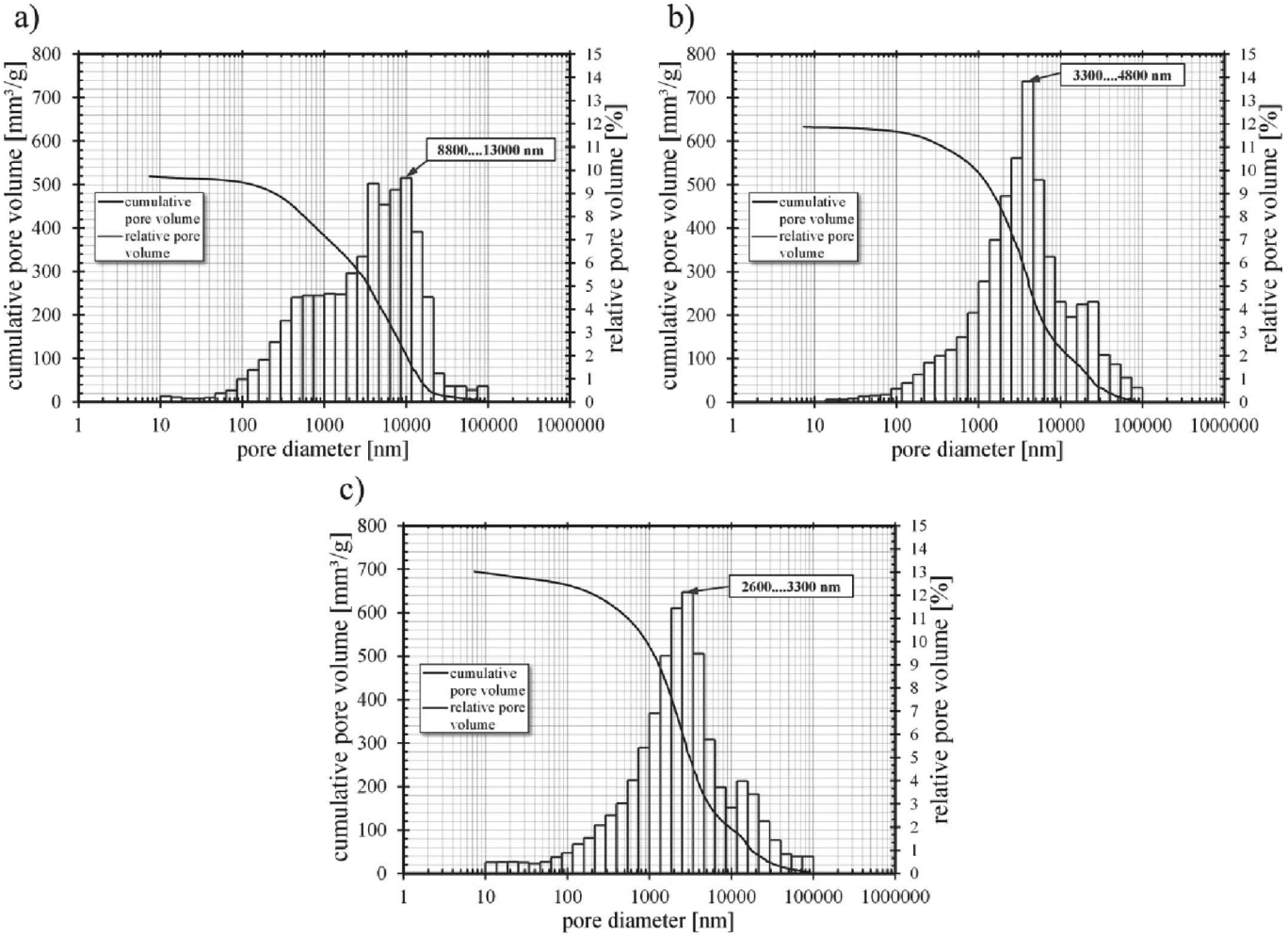

Fig. 7: Pore size distribution after water + thermal debinding process: (a) feedstock system FS-1, (b) feedstock system FS-2 and (c) feedstock system FS-3, measured by means of mercury intrusion porosimetry acc. to DIN 66133.

Table 3: Modal and average pore size as well as porosity measured by means of mercury intrusion porosimetry in comparison to open porosity measured with the Archimedes method.

Feedstock	[a]modal pore diameter	[a]average pore diameter	[a]open porosity	[b]open porosity
	[nm]	[nm]	[vol.%]	[vol.%]
FS 1	4169.9	484.2	47.59	38.91
FS-2	4115.3	820.0	52.76	4100
FS-3	2037.4	343.0	52.45	46.00

[a] Measured by means of mercury intrusion porosimetry acc. to DIN 66133 and calculated with the pore shape model "cylindrical". Modal and average diameter is defined as four times total pore volume divided by the surface area.
[b] Measured with the Archimedes method acc. to DIN 51918.

(4) Microstructure of C-SiSiC materials

In Fig. 9 SEM-micrographs (SE) of polished cross-sections after siliconization of feedstock system FS-1 (Fig. 8a, b), feedstock system FS-2 (Fig. 8c, d) and feedstock system FS-3 (Fig. 8e, f) are presented. All C-SiSiC materials show a relatively homogeneous three-phase microstructure consisting of reaction-formed silicon carbide (SiC), residual silicon (Si) and unconverted carbon (C) resulting from the carbon preform matrix. The exothermic reaction between liquid silicon and solid carbon and the associated formation of silicon carbide take place on the basis of main reaction mechanism acc. to the following equations 5 – 8:

$$Si_{(l)} + C_{(s)} \rightarrow SiC_{(s)} \quad (4)$$

$$Si_{(g)} + C_{(s)} \rightarrow SiC_{(s)} \quad (5)$$

$$Si_{(s)} + C_{(s)} \rightarrow SiC_{(s)} \quad (6)$$

which are referred to as liquid-solid (Eq. 4), gas-solid (Eq. 5) and solid-solid (Eq. 6) reaction.

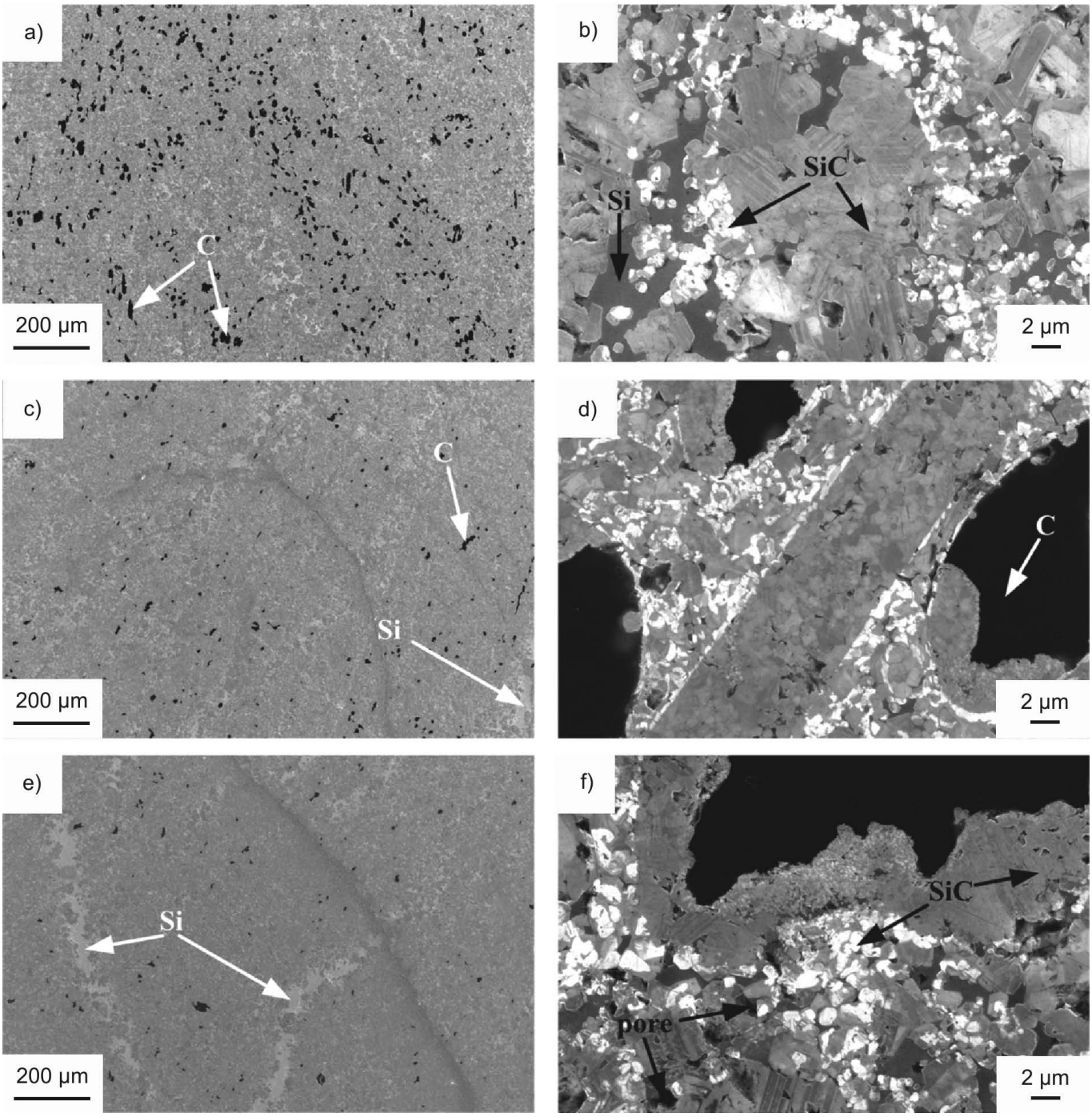

Fig. 8: SEM-micrographs (SE) of polished cross sections for C-SiSiC material based on FS-1 (a, b), FS-2 (c, d) and FS-3 (e, f).

The C-SiSiC material based on starting composition FS-1 (Fig. 8 a, b) shows a high content of unconverted carbon (~ 6 – 10 vol%). The residual carbon was well distributed over the observed cross-sections. Numerous relatively large (10 – 20 µm) carbon residues consisting of unconverted carbon fibers and pitch coke clusters are visible, which have an apparently denser carbon structure than the completely converted activated carbon particles. Generally, unconverted carbon is an indication for insufficient porosity and inaccessible dense carbon matrix of carbon preform. The second effect governing the reactivity is the crystal structure, the pitch coke formed from the polyaromatic semi-coke precursor and the pitch fibers made from chemically similar precursors are well crystallized and thus relatively unreactive. The low open porosity and the large pore diameters of FS-1 carbon preform are the reasons for a resulting C-SiSiC material with high residual carbon and also low silicon carbide content (~ 71 vol%). In contrast to that, the C-SiSiC materials based on FS-2 (Fig. 8 c, d) and FS-3 (Fig. 9 e, f) showed lower residual carbon contents (~ 0 – 3 vol%) and a marginally larger silicon carbide conversion degree than FS-1. Approximately 75 vol% silicon carbide yield could be realized with the material systems FS-2 and FS-3.

All microstructures showed large connected areas of residual silicon after the siliconization process. This effect

was more significant for the C-SiSiC materials of FS-2 and FS-3 (Fig. 8 c, e) with higher contents of thermoplastic binder in the preform stage and thus higher porosity in the debinded material compared to FS-1. The increased binder contents caused binder clusters, which in turn induced large pore clusters after the debinding process. These large and compact porosity areas appear only sporadically as the pore size distribution analyses showed. In these large pores no silicon carbide can be formed and large patches of residual silicon can be seen.

The main difference in residual carbon and silicon ratio of microstructure compositions strongly correlates to the difference in densities, measured with the Archimedes method and helium pycnometer (Table 4).

The highly dense silicon carbide matrix of the three material systems consists of silicon carbide grains with grain sizes ranging between 200 nm and 2 μm. Only small fractions of pores were detected. These isolated pores probably result from preparation defects. The β-SiC grain formation depends on the initial location of the reaction components silicon and carbon matrix. Thus, numerous fine SiC grains of nano- or submicron-size up to 1 μm are formed inside areas of high residual silicon content. This is due to the spontaneous crystallization of SiC formed from carbon which has diffused into the liquid silicon. In the carbon matrix, increased occurrence of larger SiC grains (>1 μm) was detected. The reason is an abrupt reaction in the contact zone of liquid silicon and dense carbon and the associated formation of a starting SiC layer (Fig. 8 f). This layer consists of growing SiC grains which coalesce over the reaction time. In the case of residual carbon, resulting from dense carbon fibers or pitch-coke clusters, the thickness of β-SiC layer measured with SEM micrographs was 6 – 10 μm, respectively. That correlates very well with the investigation of R. Voytovych *et al.* for the reaction-formed SiC between silicon and vitreous carbon [9].

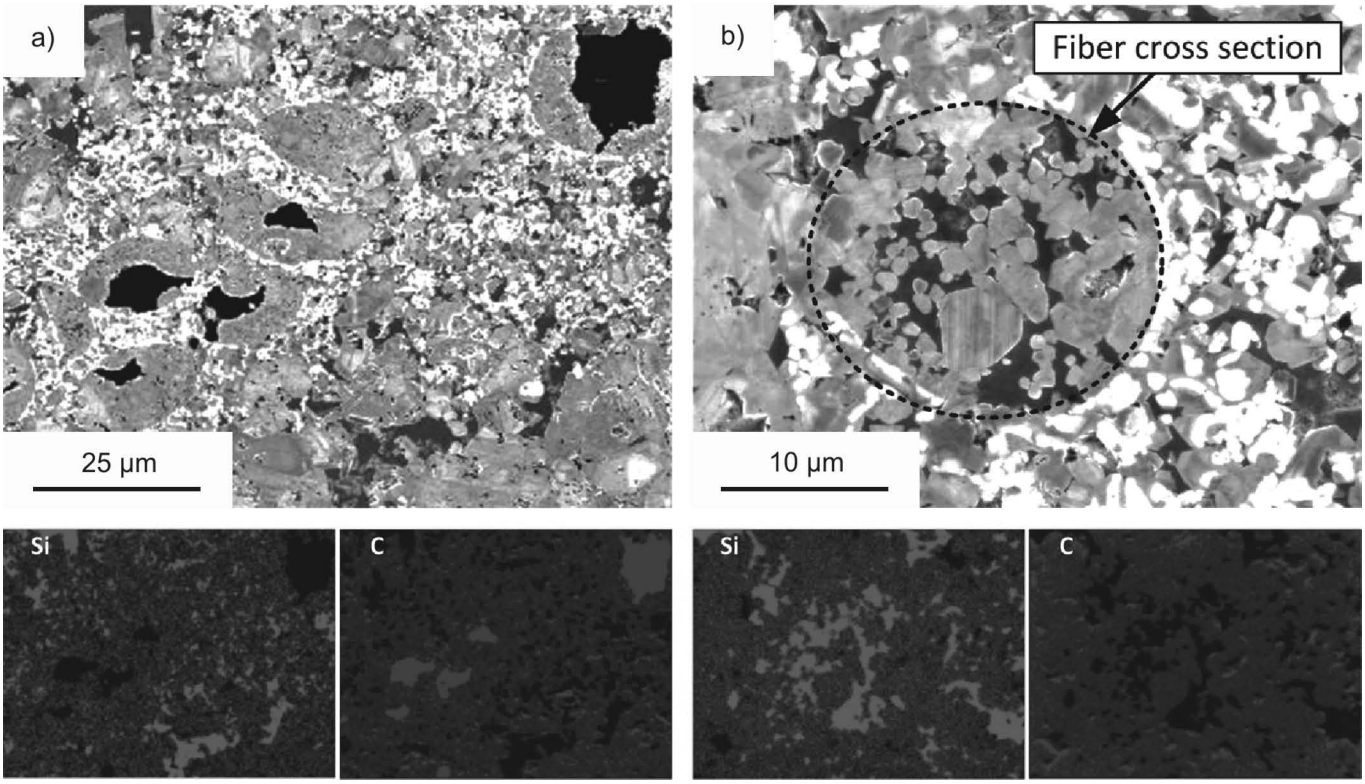

Fig. 9: EDS-mapping of typical C-SiSiC microstructures after siliconization (T > 1450 °C): (a) three-phase microstructure C-SiSiC, (b) mainly two-phase microstructure SiSiC. Bright color indicates location of dedicated element.

Table 4: Density of C-SiSiC material based on feedstock systems FS-1, FS-2 and FS-3 after water + thermal-debinding and direct thermal-debinding routes, measured with the helium pycnometer as well as with the Archimedes method.

C-SiSiC	[a]density based on WD+TD	[b]density based on WD+TD	[a]density based on TD	[b]density based on TD
	[g/cm^3]	[g/cm^3]	[g/cm^3]	[g/cm^3]
FS-1	2.88	2.88	2.93	2.94
FS-2	2.97	2.99	2.98	3.04
FS-3	3.01	3.01	2.97	2.99

[a] Density measured with the helium pycnometer acc. to ISO 1183
[b] Density measured the Archimedes method acc. to DIN 51918.

In Fig. 9 EDS-mappings of typical C-SiSiC microstructures based on the developed feedstock systems after siliconization are shown. Bright color indicates the location of the corresponding elements in the sub-figures. This measurement shows more detailed information on the elemental distribution and can give some hints how the microstructures of these material systems should be adjusted to obtain higher homogeneity. Besides the pure silicon carbide matrix (SiC), a two-phase (C-SiC, Si-SiC) and three-phase (C-SiSiC) matrix could arise. Thus, only the elements silicon (Si) and carbon (C) are shown.

The microstructure formation is strongly affected by the relation between carbon matrix and apparent as well as closed porosity in the carbon preform stage. If the volume fractions of carbon and porosity are inconsistent with the silicon carbide volume which is formed from the elements, either residual carbon or silicon remain in microstructure (Fig. 9 a). This effect is amplified by the existence of inaccessible and dense or unreactive carbon clusters in the carbon preforms and increases the residual carbon content of the final ceramic microstructure. Another case is shown in Fig. 9 b, where the dotted circle outlines a fully degraded carbon fiber. The carbon of the fiber has been totally dissipated for the formation of silicon carbide. Thus, one part of fiber carbon diffuses through the starting silicon carbide layer, producing a verge of fine SiC grain crystallized in liquid silicon. The remaining carbon reacts with the silicon, which diffuses into the carbon fiber matrix area forming a non-dense granular structure.

(5) Tribological behavior of C-SiSiC materials

Dry sliding wear behavior of C-SiSiC materials was evaluated on a pin-on-disk tribometer. A cemented carbide ball of 5 mm diameter was reciprocally slid in translational direction with a sliding velocity of 0.012 m/s. The stroke length of the oscillating motion was 10 mm, the final travelling distance was 2 km for all test materials. The applied normal load FN was kept constant at 20 N. The resulting friction coefficient was recorded during the whole measurement time. Before wear testing all specimens were rinsed ultrasonically in acetone and cleared with pressurized air. All tests were performed under the same conditions and according to the same procedure.

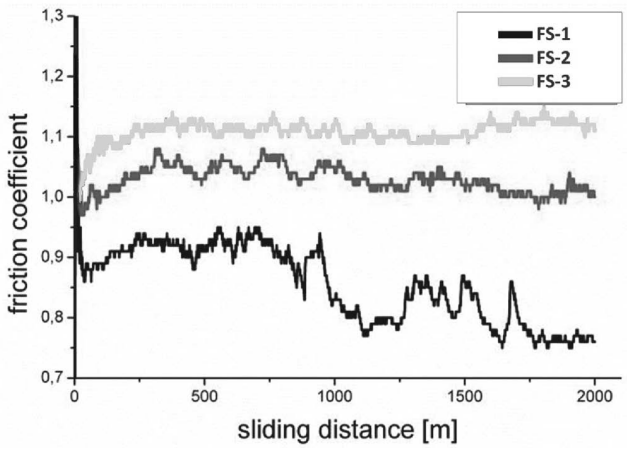

Fig. 10: Friction coefficients of tested specimen as a function of sliding distances.

Fig. 10 shows friction coefficients as a function of sliding distance. Because of the huge amount of values, data points of friction coefficients represent average values of one-minute intervals. Even though friction coefficients strongly dependent on substrate materials and the counter body, the machine set-up can influence measurements so that coefficients should not be taken as absolute values.

The first 250 meters of sliding can be attributed to a first polishing effect of the specimen surface and microflattening of the ball. After this effect has been leveled out, the friction coefficient curves show distinct differences with proceeding sliding distance. Generally friction coefficients 2 and 3 are higher than the resulting coefficient of C-SiSiC 1 (based on FS-1 material). Median friction coefficients 2 and 3 are 0.95 and 1.03 respectively, while the lowest coefficient of 0.85 was recorded for specimen C-SiSiC 1. Moreover the resulting friction coefficient of the C-SiSiC 1 specimen decreases, while coefficients of C-SiSiC 2 and 3 remain on a constant level. This phenomenon can be attributed to the different content of unconverted carbon remaining in the composite. Whereas larger amounts of carbon were converted in Material 2 and 3, the higher amount of residual carbon acts as a lubricant, resulting in lower friction coefficients. This is also the reason for higher variation of friction curves as C-SiSiC 1 shows inhomogeneous distribution of unconverted carbon and parts of converted SiC. Additionally, volumes of abrasion traces were analyzed with a surface profilometer. The wear volume of C-SiSiC 1 was slightly smaller than the wear volumes of C-SiSiC 2 and 3 (not shown here), indicating that friction coefficients and wear can be tailored by means of different material compositions and processing parameters.

IV. Conclusions

On the basis of the data reported and discussed in section III, the following conclusions can be drawn:

1. The processability of carbon-based feedstock systems via thermoplastic extrusion or injection molding process is dependent on the relation between the thermoplastic binder and carbon filler content: Feedstock system FS-1 showed insufficient processability via the extrusion process caused by a small binder volume fraction (36 vol%) and correspondingly high feedstock viscosity. Based on the mixtures of fillers used, feedstock systems require thermoplastic binder contents above ~ 40 vol% (FS-2/45 vol% and FS-3/48.3 vol%) to obtain low viscosities, which are necessary for the extrusion process.

2. After the extrusion and carbonization process, the carbon preforms showed sufficient structural strength for further processing with the liquid silicon infiltration process (LSI). The sinterable semi-coke forms a pitch coke backbone upon pyrolysis and thus acts as a permanent binder. It provides sufficient strength of the carbon intermediates. Partial substitution of semi-coke with activated carbon in FS-3 results in a significant strength decrease of the carbon preform compared to FS-1 and FS-2.

3. The morphology of carbon fillers and the thermoplastic binder content as well as the distribution of the constituents strongly influence pore distribution and average

pore sizes in carbon preforms after the debinding process: All three material systems exhibit large pores in carbon preform stage, which were caused by the debinded thermoplastic binder. This indicates a need for improved feedstock homogenization. The pores in FS-2 and FS-3 were more homogenously distributed and smaller than in material system FS-1, which is partially attributed to the preground semi-coke in FS-2 and FS-3. In FS-3 carbon preform, pores are significantly smaller (average pore diameter of 343 nm at an open porosity between 46 – 52 vol%), which is a result of increased activated carbon content and thus an increase in nano-size pores.

4. After the siliconization process, the material systems consist of a three-phase C-SiSiC microstructure. The residual carbon and silicon are embedded in a relatively dense SiC matrix with SiC grain sizes between 200 nm and 2 μm. FS-1 shows a high content of unconverted carbon (~ 6 – 10 vol%), which is primarily caused by the larger semi-coke particles that were used in contrast to the ground semi-coke in FS-2 and FS-3. This fact also affected the SiC yield, which was ~ 71 vol% for FS-1 and ~ 75 vol% for FS-2 as well as FS-3. The formation of large areas of free silicon has been increasingly noticeable for FS-2 and FS-3 compared to FS-1 with lower thermoplastic binder content.

5. Wear behavior of three tested C-SiSiC materials showed distinct differences in resulting friction coefficients, thus wear behavior. This implies that tribological behavior can be tailored within limits. The C-SiSiC material based on FS-1 shows the lowest friction coefficient of the three material systems. This fact is attributed to the higher residual carbon content of FS-1 material system. In this case, residual carbon acts as a lubricant. However, longer travelling distances on more homogeneous materials should be carried out in order to qualitatively and quantitatively compare different wear behavior of developed materials.

The studies have shown that the initial composition strongly influences the process characteristics of the extrusion process as well as the properties of subsequently formed carbon intermediates and final C-SiSiC materials. In order to retain processability over the whole process chain, the ratio between the three filler materials and the binder must be adjusted carefully and a certain relation between porosity and carbon matrix is required. The focus for future work will be the further investigation of the recipes influencing the shaping process and a more detailed study of interaction of binder and carbon fillers with the porosity and carbon matrix evolution.

Acknowledgements

This work was financially supported by German Aerospace Center, Institute of Structures and Design as well as the University of Stuttgart, Institute for Manufacturing Technologies of Ceramic Components and Composites. The authors gratefully acknowledge Mrs Gudrun Steinhilber (DLR) for conducting mercury intrusion porosimetry measurements.

References

1 Kollenberg, W.; Technische Keramik, Vulkan-Verlag GmbH, Essen, (2004) (in German)

2 Liu, G., Li, J., Shan, Y., Xu, J.: Highly dense β-SiC ceramics with submicron grains prepared by sintering of nanocrystalline powders, *Scripta Mater.*, **67**, 416 – 41, (2012).

3 Gadow, R.: The siliconization of carbon, (in German), Dissertation, University of Karlsruhe, (1986).

4 Wang, Y., Tan, S.,Jiang, D.: The fabrication of reaction-formed silicon carbide with controlled microstructure by infiltrating a pure carbon preform with molten Si, *Ceram. Int.*, (2004)

5 Wang, Y., Tan, S., Jiang, D.: The effect of porous carbon preform and the infiltration process on the properties of reaction-formed SiC, *Carbon*, **42**, 1833 – 1839, (2004).

6 Singh, M., Behrendt, D.: Reactive melt infiltration of silicon-molybdenum alloys into microporous carbon preforms, *Mater. Sci. Eng. A*, **194**, 193 – 200, **1995**

7 Kumar, S., Kumar, A., Devi, R., Shukla, A., Gupta, A.: Capillary infiltration studies of liquids into 3D-stitched C-C preforms: part B: kinetics of silicon infiltration, *J. Eur. Ceram. Soc.*, **29**, 2651 – 2657, (2009).

8 Kumar, S., Kumar, A., Shukla, A., Gupta, A., Devi, R.: Capillary infiltration studies of liquids into 3D-stitched C-C preforms: part A: internal pore characterization by solvent infiltration, mercury porosimetry, and permeability studies, *J. Eur. Ceram. Soc.*, **29**, 2643 – 2650, (2009).

9 Voytovych, R., Israel, R., Calderon, N., Hodaj, F., Eustathopoulos, N.: Reactivity between liquid si or si alloys and graphite, *J. Eur. Ceram. Soc.*, **32**, 3825 – 3835, (2012).

10 Magnant, J., Maillé, L., Pailler, R., Ichard, J.-C., Guette, A., Rebillat, F., Philippe, E.: Carbon fiber/reaction-bonded carbide matrix for composite materials – manufacture and characterization, *J. Eur. Ceram. Soc.*, **32**, 4497 – 4505, (2012).

11 Margiotta, J.C., Zhang, D., Nagle, D.C., Feeser, C.E.: Formation of dense silicon carbide by liquid silicon infiltration of carbon with engineered structure, *J. Mater. Res.*, **23**, 1237 – 1248, (2008).

12 Margiotta, J.C. *et al.*: Formation of dense silicon carbide by liquid silicon infiltration of carbon with engineered structure, *Cambridge Journal*, (2004).

13 Nelson, E.S., Colella, P.: Parametric study of reactive melt infiltration, *Proceedings of the 1999 International Mechanical Engineering Congress and Exposition,* (1999).

14 Xu, S., Qiao, G., Li, D., Yang, H., Liu, Y., Lu, T.: Reaction forming of silicon carbide ceramic using phenolic resin derived porous carbon preform, *J. Eur. Ceram. Soc.*, **29**, 2395 – 2402, (2009).

15 Li, S., Zhang, Y., Han, J., Zhou, Y.; Effect of carbon particle and carbon fiber on the microstructure and mechanical properties of short fiber reinforced reaction bonded silicon carbide composite, *J. Eur. Ceram. Soc.,* (2012).

16 Li, S., Zhang, Y., Han, J., Zhou, Y.: Random chopped fibers in reaction bonded SiC composite: morphology, etching and reinforcing properties, *Mater. Sci. Eng. A*, **551**, 104 – 10, (2012).

17 Weber, S. *et al.*: Microstructures and physical properties of biomorphic SiSiC ceramics manufactured via LSI-technique. *Proceedings of the 36th International Conference and Expo on Advanced Ceramics and Composites*, San Diego, (2012).

18 Weber, S. *et al.*.: Activated carbon based compound systems for the manufacture of complex shaped SiSiC structures, (in German), *Deutsche Keramische Gesellschaft, Arbeitskreis "Kohlenstoff" (AKK)*, (2012).

[19] Lara, A., Muñoz, A., Castillo-Rodríguez, M., Domínguez-Rodríguez, A.: High-temperature compressive creep of spark-plasma sintered additive-free polycrystalline β-SiC, *J. Eur. Ceram. Soc*., **32**, 3445 – 3451, (2012).

[20] Jang, B.K., Sakka, Y.: Influence of microstructure on the thermophysical properties of sintered SiC ceramics, *J. Alloy. Compd.*, **463**, 493 – 497, (2008).

[21] Malinge, A., Coupé, A., Petitcorps, Y.L., Pailler, R.: Pressureless sintering of beta silicon carbide nanoparticles, *J. Eur. Ceram. Soc.,* (2012)

[22] Petutschnigg, A.: Development of a shaping process for wood-based green bodies for the production of biogenic SiC ceramics, (in German), Federal Ministry for Transport, Innovation and Technology, 39/2012, **2012**

[23] Kern, F., Gadow, R.; Extrusion and injection molding of ceramic micro and nanocomposites, *Inter. J. Mater. Forming,* 01/2009; 2:609 – 612, (2009).

[24] Kern, F., Gadow, R.: Model assisted optimization of debindering and sintering processes in ceramic injection molding, *Stuttgarter Kunstoffkolloqium,* (2011).